Extending the Usability of Radiometer Ocean Surface Wind Measurements to All-Weather Conditions for NOAA Operations: Application to AMSR2

Suleiman Alsweiss, *Senior Member, IEEE*, Zorana Jelenak, *Member, IEEE*, and Paul S. Chang, *Senior Member, IEEE*

***Abstract*— This article describes the development and validation of a statistical algorithm to retrieve global all-weather sea surface wind speed (GAWS) from microwave radiometers in operational environment. Measurements from the Advanced Microwave Scanning Radiometer-2 (AMSR2) are utilized to demonstrate the efficacy of the new all-weather wind speed data product. The GAWS algorithm exploits the linear combination of dual-polarized radiometer channels to significantly mitigate the effect of rain contamination while maintaining sensitivity to all wind speed regimes from global winds to tropical cyclone (TC) conditions. The GAWS algorithm was developed using ≈1000 AMSR2 orbits from 2013 to 2021 covering all possible variations of brightness temperatures and wind speeds. The Global Data Assimilation System (GDAS) and the Hurricane Weather Research and Forecasting Model (HWRF) were used as the assumed surface truth for training and validation. Results from comprehensive quantitative and qualitative analyses show that the GAWS retrievals are less susceptible to rain than standard microwave radiometer wind speeds and can reach hurricane force winds up to hurricane category 5 (>70 m/s).**

***Index Terms*— Advanced Microwave Scanning Radiometer-2 (AMSR2), all weather, microwave radiometers, ocean surface wind speed, rain, tropical cyclones (TCs).**

I. Introduction

MICROWAVE radiometers are special sensors designed to collect Earth's thermally emitted electromagnetic (EM) radiation at a certain frequency (f), earth incidence angle (EIA), and polarization (P) [1], [2], [3]. They are equipped with multiple receiving channels that are sensitive to specific atmospheric and surface parameters. These geophysical quantities modulate the brightness temperatures (Tbs) before being collected by the radiometer's antennas system at the top of the atmosphere. An inversion process is then used to infer these geophysical parameters using calibrated Tbs from the appropriate radiometer channels [4], [5], [6], [7], [8].

Among all sea surface parameters, sea surface winds (SSWs) are considered the largest source of momentum for ocean surface. They affect the full range of ocean movement from individual surface waves to complete current systems. They also regulate the interaction between the atmosphere and the ocean via modulating the air–sea exchanges of heat, moisture, and gases [9], [10].

Under rain-free conditions, the strong correlation between microwave emission and surface roughness leads to accurate SSW retrievals from Tbs (within 1-m/s accuracy) [11]. In contrast, the task of retrieving SSW from Tbs in the presence of precipitation is much more challenging and leads to erroneous (often exaggerated) SSW retrievals. This can be mainly attributed to the following reasons [12].

1) Rain increases the atmospheric attenuation, which, in turn, decreases the signal-to-noise ratio making Tbs less sensitive to SSW.
2) Rain and wind speed signatures on Tbs are very similar; thus, the existence of rain within the radiometer instantaneous field of view (IFOV) has comparable effect on Tbs as an increase in wind speed.
3) Physical retrieval algorithms depend on radiative transfer models (RTMs). Due to the high variability of rain [13], it is very difficult for the RTM to accurately model Tbs under rain conditions.

However, for many applications, such as cyclogenesis and storms tracking, the ability to retrieve SSW in the presence of rain is valuable. The new global all-weather SSW algorithm presented in this article, hereafter referred to as global all-weather sea surface wind speed (GAWS), is an attempt to mitigate rain contamination of microwave radiometer measurements for the purpose of retrieving global SSW under all-weather conditions, including tropical cyclones (TCs) and extra-TCs (ETCs).

In May 2012, the Japanese Aerospace Exploration Agency (JAXA) launched the Global Change Observation Mission-Water (GCOM-W1) with the Advanced Microwave

Manuscript received 24 October 2022; revised 26 February 2023; accepted 4 April 2023. Date of publication 13 April 2023; date of current version 28 April 2023. This work was performed and supported under Grant ST13301CQ0050/1332KP22FNEED0042. *(Corresponding author: Suleiman Alsweiss.)*

Suleiman Alsweiss is with Global Science and Technology Inc. (GST), Greenbelt, MD 20770 USA (e-mail: suleiman.alsweiss@noaa.gov).

Zorana Jelenak is with University Corporation for Atmospheric Research (UCAR), Boulder, CO 80307 USA (e-mail: zorana.jelenak@noaa.gov).

Paul S. Chang is with National Oceanic and Atmospheric Administration (NOAA)/National Environmental Satellite, Data and Information Service (NESDIS)/Center for Satellite Applications and Research (STAR)/Satellite Oceanography and Climatology Division (SOCD), College Park, MD 20740 USA (e-mail: paul.s.chang@noaa.gov).

Digital Object Identifier 10.1109/TGRS.2023.3266772

TABLE I
AMSR2 INSTRUMENT SPECIFICATIONS

Center Freq. (GHz)	3dB Beam Width (deg.)	Ground IFOV (km)	Sampling Interval (km)
6.925/7.3	1.8	35×62	
10.65	1.2	24×42	
18.7	0.65	14×22	10
23.8	0.75	15×26	
36.5	0.35	7×12	
89.0	0.15	3×5	5

Scanning Radiometer-2 (AMSR2) onboard [14], [15]. AMSR2 has a full suite of dual-polarized channels ranging from 6 to 89 GHz providing sufficient information to retrieve ocean surface and atmospheric parameters. Thus, AMSR2 is used in this study as an application of the GAWS retrieval algorithm.

The remaining of this article is organized as follows. Section II provides an instrument overview of AMSR2 and its operating characteristics. Section III explains the steps taken in the development of the GAWS retrieval algorithm. Section IV presents the assessment and performance evaluation of the GAWS algorithm when applied to AMSR2 measurements and compared with numerical weather models and other data products. Finally, Section V summarizes our findings and conclusions.

II. AMSR2 INSTRUMENT OVERVIEW

AMSR2, onboard of GCOM-W, measures dual-polarized [vertical (V-pol) and horizontal (H-pol)] Tbs at 6.9, 7.3, 10.65, 18.7, 23.8, 36.5, and 89.0 GHz with an IFOV spatial resolution that varies inversely with frequency. It is a sun-synchronous orbiter (local time of ascending node 13:30) at an altitude of ≈700 km and a conical scanning geometry acquiring measurements along a semicircular pattern in front of the spacecraft. It operates at a nominal EIA of 55°, resulting in a wide swath of 1450 km [14], [15] covering more than 99% of the Earth every two days.

AMSR2 shares most of AMSR-E [15], [16] characteristics with multiple enhancements, specifically: the addition of the 7.3-GHz channels [for the detection of C-band radio frequency interference (RFI)], 12-bit quantization for all channels, 2.0-m aperture diameter antenna (compared with the 1.6-m diameter of AMSR-E) that completes one full rotation every 1.5 s, and improvements in the calibration system [15]. The summarized instrument specifications of AMSR2 are shown in Table I.

AMSR2 calibrated Tbs [17] are used to generate a suite of oceanic environmental data records (EDRs), including cloud liquid water (CLW), total precipitable water (TPW), precipitation [18], sea surface temperature (SST) [6], and SSW [19]. In addition, two derived products are also provided, namely: SST anomaly and TPW percentage normal. A near-real-time presentation of AMSR2 advanced satellite data products can be obtained from [20].

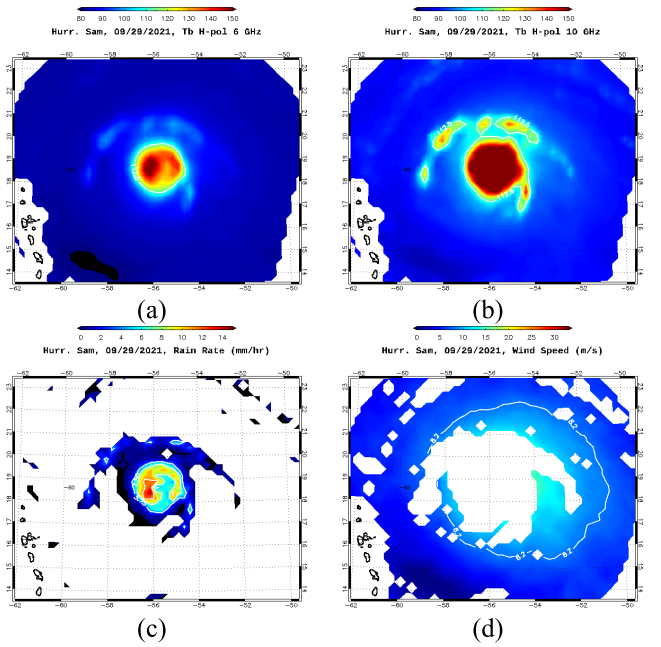

Fig. 1. AMSR2 pass over Hurricane Sam (29 September, 2021) showing (a) AMSR2 6-GHz H-pol brightness temperature, (b) AMSR2 10-GHz H-pol brightness temperature, (c) AMSR2 precipitation, and (d) standard wind speed retrievals from AMSR2 where gaps are flagged retrievals due to rain contamination.

III. ALGORITHM DESCRIPTION

The accuracy of standard SSW retrievals from microwave radiometers tends to degrade rapidly in the presence of rain. As a result, retrievals from rainy scenes are often flagged leaving considerable gaps in areas of tropical convection, such as TCs and ETCs. Fig. 1 demonstrates the rain contamination effect on Tb measurements using AMSR2 pass over Hurricane Sam (29 September, 2021), where warm colors denote higher Tb values and cold colors for lower Tb values. Fig. 1(a) and (b) shows AMSR2 6- and 10-GHz H-pol Tb in kelvin, respectively, and Fig. 1(c) shows AMSR2 retrieved rain rate (RR) in mm/h for comparison. It is clear how observed Tbs [Fig. 1(a) and (b)] exhibit a strong signature of rain when compared with Fig. 1(c). When used in standard retrieval algorithms, Tbs from rainy scenes lead to erroneous SSW retrievals resulting in gaps when flagged, as shown in Fig. 1(d).

Thus, the GAWS algorithm attempts to extend the usability of microwave radiometer measurements for the purpose of retrieving global SSW to all-weather conditions and wind speed regimes. It differs from standard SSW retrieval algorithms by being a statistical-based algorithm that does not rely on an RTM. Also, it exploits a linear combination of multispectral dual-polarized Tbs that keeps rain signature relatively small even in heavy rain. This section will describe in detail the development of GAWS retrieval algorithm using AMSR2 measurements.

A. Datasets

AMSR2 acquires Tbs from 12 different channels. These Tbs are obtained from JAXA's Level 1B version 1.1 (GW1AM2 L1B v1.1, indicated hereafter as AMSR2 L1B). In addition

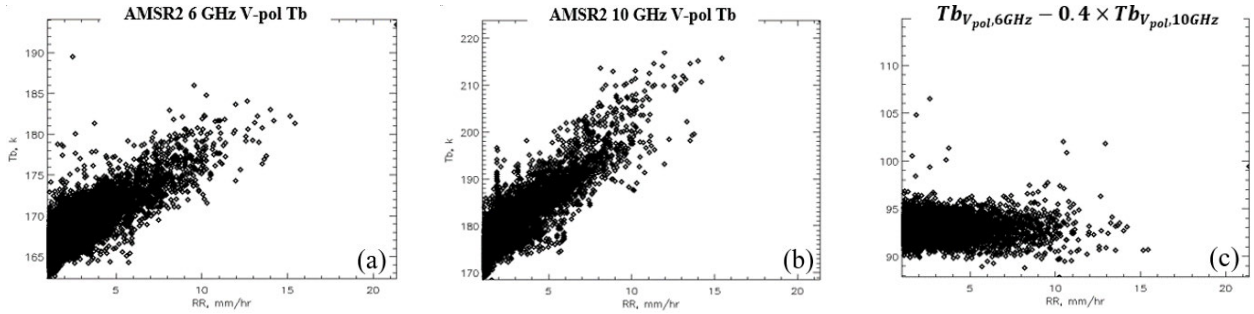

Fig. 2. Linear combination of AMSR2 (a) 6- and (b) 10-GHz V-pol brightness temperatures resulting in (c) that is much less sensitive to rain.

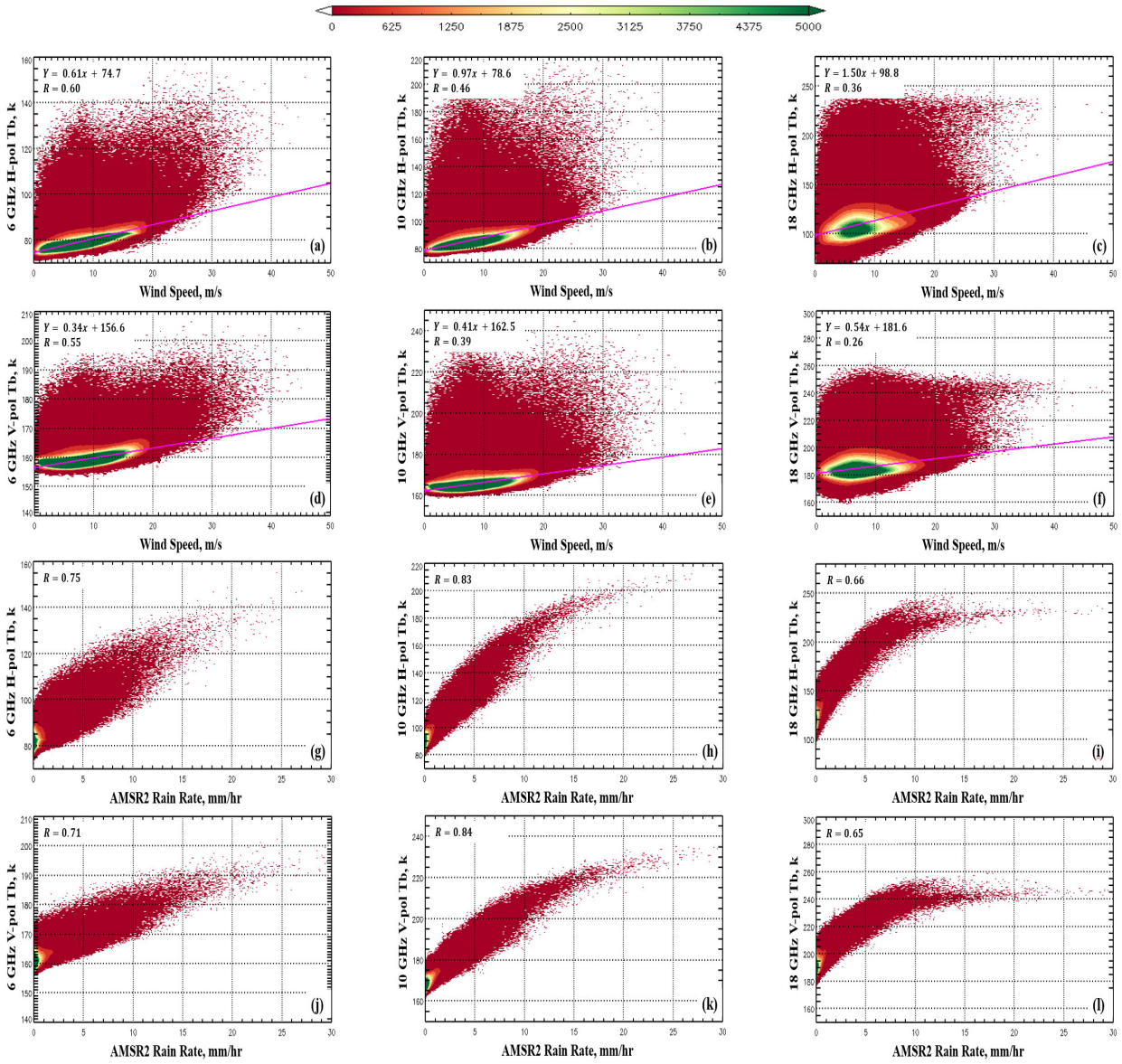

Fig. 3. Sensitivity of AMSR2 H- and V-pol 6-GHz channels (first column), 10-GHz channels (second column), and 18-GHz channels (third column) to (a)–(f) wind speed and (g)–(l) RR.

to observed Tbs, this data product contains the observation position (latitude and longitude), time, and orbit information. A detailed description of AMSR2 L1B data product is available online in [21]. It is worth noting that the GAWS retrieval algorithm makes use of the calibrated AMSR2 L1B Tbs as described in [17] to reduce post-launch calibration biases.

For training and validation purposes, the Global Data Assimilation System (GDAS) [22], [23] and the Hurricane

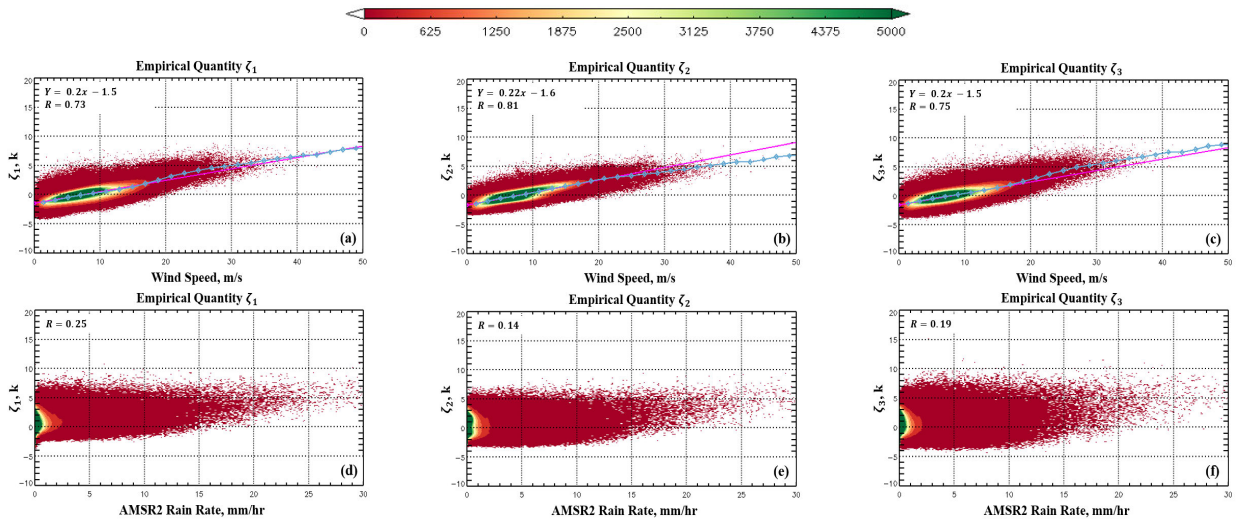

Fig. 4. Empirical quantities (ζ_1, ζ_2, and ζ_3, in kelvin) as a function of (a)–(c) wind speed in m/s and (d)–(f) AMSR2 RR in mm/h. Color indicates the number of points as shown in the color bar.

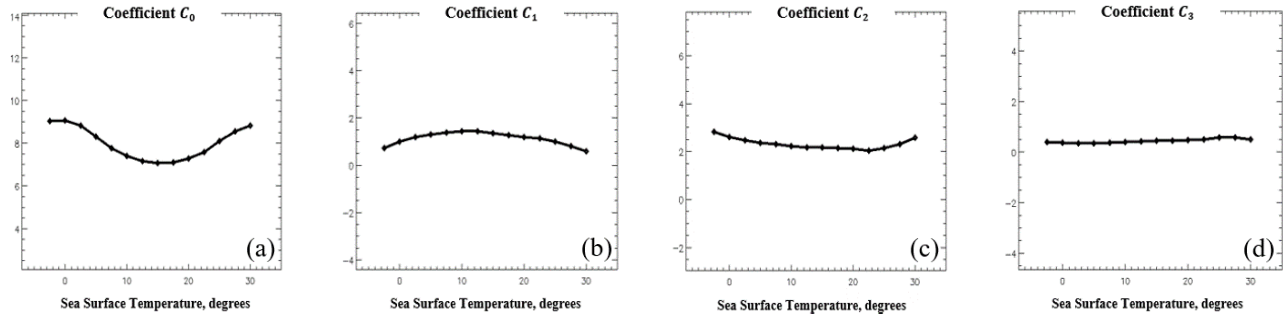

Fig. 5. First-stage regression coefficients (a) C_0, (b) C_1, (c) C_2, and (d) C_3).

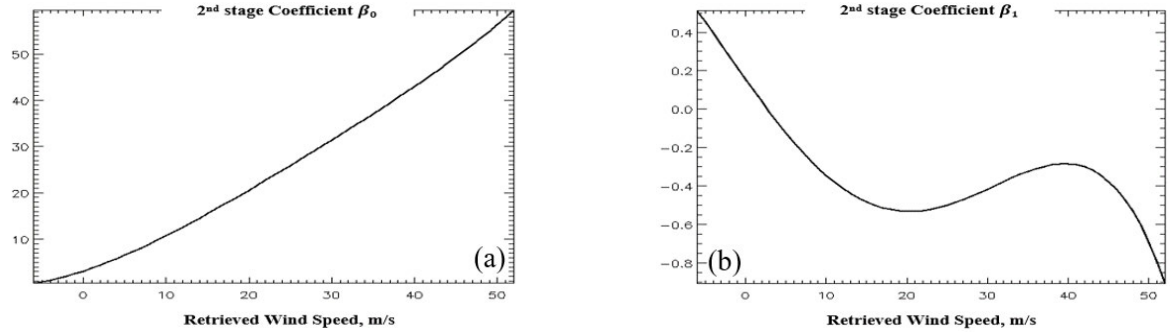

Fig. 6. Second-stage regression coefficients (a) β_0 and (b) β_1, as a function of wind speed retrievals from first stage.

Weather Research and Forecasting Model (HWRF) [24], [25] were used as the assumed surface truth after being spatially and temporally interpolated to AMSR2 observations' time and location.

GDAS data are readily available every 6 h and provide a set of surface and atmospheric parameters, including the 10-m U and V wind components. The assimilation system used by GDAS blends data from multiple sources (i.e., surface observations, balloon data, wind profiler data, aircraft reports, buoy observations, radar observations, and satellite observations) into a gridded 3-D model space. In this study, we used the 0.25° resolution GDAS data, which consist of 1440 × 720 longitude/latitude grid boxes.

The HWRF model is an evolving system that was developed at National Oceanic and Atmospheric Administration (NOAA)'s National Centers for Environmental Prediction (NCEP). It provides numerical guidance for operational forecasters at all oceanic basins for the forecasting of TCs' track, intensity, and structure. HWRF is triply nested, providing three different gridded domains that encompass the location of the storm at each analysis time: one large parent domain and two smaller nested domains with smaller area coverage and higher

resolution than the parent domain. In our analysis, we used the middle nest domain "*d*02" with a resolution closest to an AMSR2 sampling of 10 km.

For extreme winds validation, we used information from the International Best Track Archive for Climate Stewardship (IBTrACS) dataset. It was developed by the NOAA's National Climatic Data Center (NCDC) and is considered one of the most comprehensive global databases of TCs spanning from 1840 to present from over ten international forecast centers [26]. This study uses the latest version of IBTrACS (version 4.0) [27] for TCs center locations and intensities interpolated to AMSR2 acquisition times as will be described in Section IV-B.

B. Quality Control

Being a global SSW retrieval algorithm, GAWS checks for several sources of Tb contamination that can lead to erroneous SSW retrievals in rain-free or rainy conditions. Contamination due to land and ice was accounted for by flagging the contaminated areas using AMSR2 L1B land/ice mask.

Furthermore, AMSR2 ascending orbits are prone to significant sun glitter effects. For pixels experiencing sun glitter contamination (when angle between AMSR2 viewing direction and the sun glitter direction is $<25°$), the algorithm will flag these regions using sun azimuth and elevation information provided in the AMSR2 L1B data files.

Finally, the addition of the 7.3-GHz channel in AMSR2 allowed for the detection of C-band RFI. RFI signals are usually narrow banded and will only affect one of the C-band channels (6.9 or 7.3 GHz). The algorithm will flag RFI contaminated measurements if the difference between these two channels is >3 km.

C. Algorithm Development

The GAWS retrieval algorithm is a statistical-based algorithm that retrieves global ocean surface wind speeds using microwave radiometer Tbs under all-weather conditions. It employs a multistage linear regression technique that maps a set of empirically derived independent variables into SSW retrievals. Sections III-C1 and III-C2 describe the development of the GAWS algorithm and the formulation of the independent variables and the regression coefficients.

1) Independent Variables: The development of GAWS relies on finding empirical quantities that intrinsically exhibit immunity to rain contamination while maintaining sensitivity to all SSW regimes, including hurricane force winds. Meissner and Wentz [28] have shown that the linear combination of the 37-GHz H- and V-pol Tbs significantly reduces the effects of the atmospheric absorption and scattering. Later, this method was refined by Soisuvarn et al. [29] using Tbs at 10.65, 18.7, and 36.7 GHz to show that a linear combination of Tbs, expressed as "$A \times Tb_{\mathrm{Vpol}} - Tb_{\mathrm{Hpol}}$" (or $AV - H$ for short), reduces the impact of the atmospheric upwelling and reflected downwelling components of Tbs, thereby making the $AV - H$ measurements almost independent of atmospheric transmittance components, such as water vapor and CLW.

TABLE II
ATMOSPHERIC CANCELLATION COEFFICIENTS FOR AMSR2 6-, 10-, AND 18-GHZ CHANNELS

λ_V	λ_H	A_{10}	A_{18}
0.40	0.38	1.91	1.95

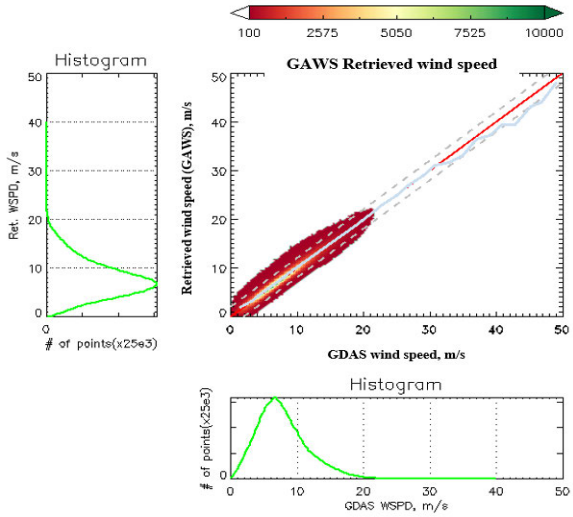

Fig. 7. Evaluation of retrieved wind speeds against GDAS. The x-axis is 0.25° resolution GDAS wind speed (m/s), and the y-axis is AMSR2 GAWS retrieved wind speed (m/s).

In this study, we will further extend the concept of linearly combining different radiometer channels to develop empirical quantities that are less susceptible to rain contamination while upholding decent sensitivity to SSW. This work is an expansion of the previously developed all-weather geophysical model function (AW-GMF) described in [30], and it narrows the focus to retrieve SSW using a unique statistical-based inversion process.

The GAWS retrieval algorithm makes use of three empirical quantities (ζ_1, ζ_2, and ζ_3), all in kelvin, resulting from the linear combinations of 6-, 10-, and 18-GHz H- and V-pol channels. The rationale for selecting these channels is that the surface emissivity and, consequently, Tbs show sensitivity to SSW with no indication that the surface signal will saturate at higher wind speeds [31], [32]. Thus, once the atmospheric attenuation is removed, the 6-, 10-, and 18-GHz H- and V-pol channels will be good candidates for retrieving SSW in all wind speed regimes. The linear combinations of these channels can be mathematically described, as shown in (1)–(3). Table II summarizes the coefficients (λ and A) used to linearly combine corresponding channels for atmospheric cancellation

$$\zeta_1 = 2 \times X_V - \mathrm{AVH}_{18}. \tag{1-a}$$

$$X_V = Tb_{\mathrm{Vpol,6\,GHz}} - \lambda_V \times Tb_{\mathrm{Vpol,10\,GHz}}. \tag{1-b}$$

$$\mathrm{AVH}_{18} = A_{18} \times Tb_{\mathrm{Vpol,18\,GHz}} - Tb_{\mathrm{Hpol,18\,GHz}}. \tag{1-c}$$

$$\zeta_2 = 2 \times X_H - \mathrm{AVH}_{18}. \tag{2-a}$$

$$X_H = Tb_{\mathrm{Hpol,6\,GHz}} - \lambda_H \times Tb_{\mathrm{Hpol,10\,GHz}}. \tag{2-b}$$

$$\zeta_3 = 2 \times X_V - \mathrm{AVH}_{10}. \tag{3-a}$$

$$\mathrm{AVH}_{10} = A_{10} \times Tb_{\mathrm{Vpol,10\,GHz}} - Tb_{\mathrm{Hpol,10\,GHz}}. \tag{3-b}$$

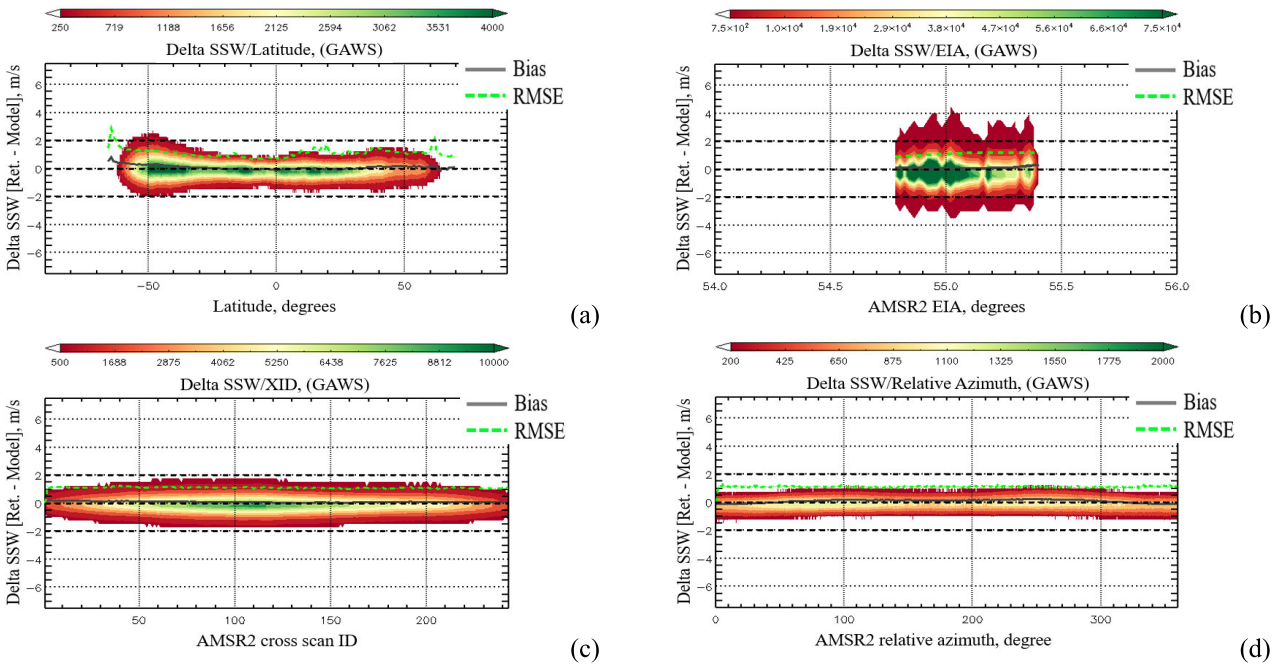

Fig. 8. AMSR2 GAWS wind speed error as a function of (a) latitude, (b) EIA, (c) cross-scan location, and (d) relative azimuth. All comparisons show a 0-m/s mean bias and <2-m/s rms error.

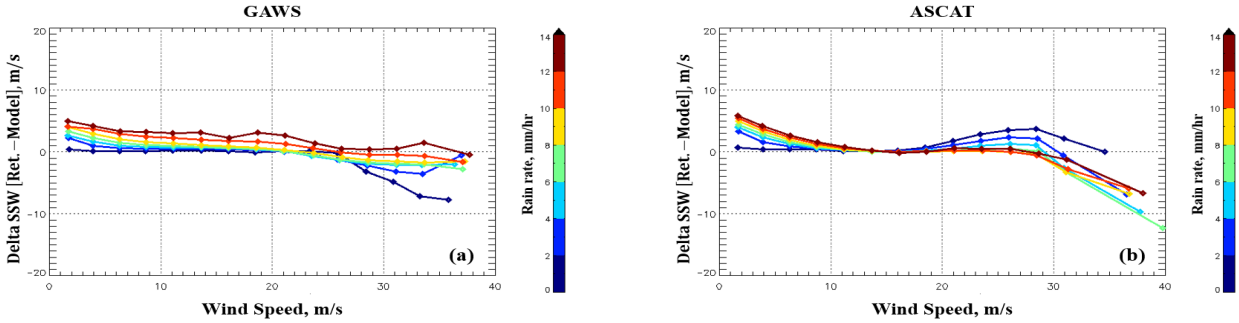

Fig. 9. Comparison of wind speed error as a function of GDAS wind speed for multiple RRs indicated by different colors for (a) AMSR2 GAWS and (b) ASCAT.

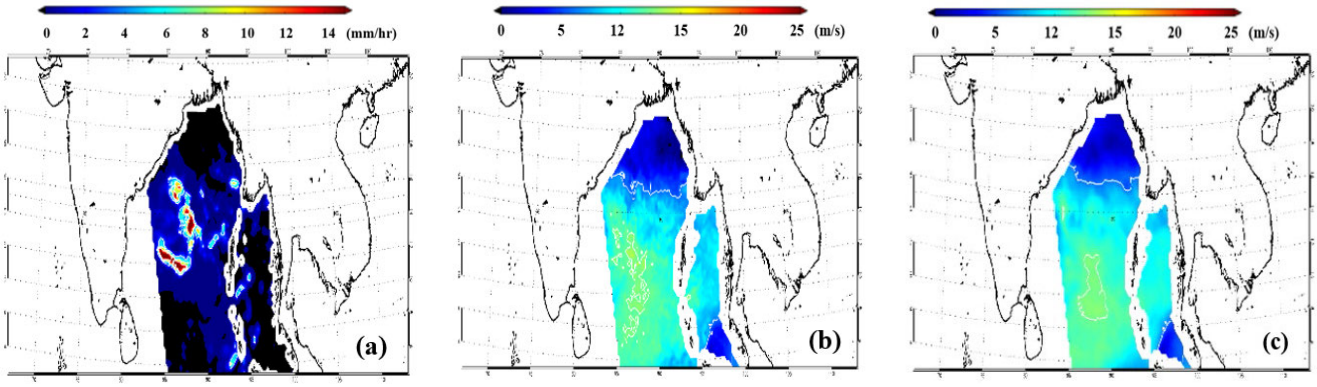

Fig. 10. Example of GAWS wind speed retrievals in rain where shows (a) AMSR2 RR (mm/h), (b) GAWS applied to AMSR2 retrievals in m/s, and (c) GDAS wind speed in m/s.

The values of λ and A were found using gradient descent, ensuring the linear combination of the corresponding channels has minimal sensitivity to rain following:

$$\frac{\partial L}{\partial \mathrm{RR}} = 0 \tag{4}$$

where L represents the different linear combinations expressed in (1-b), (1-c), (2-a), and (3-b) and RR is the rain rate in mm/h. When the partial derivative of L with respect to RR equals zero, this means that $L|_{A \text{ or } \lambda}$ is not sensitive to rain.

Fig. 2 shows a depiction of (1-b) with λ_V equals 0.4 using AMSR2 6- and 10-GHz V-pol Tbs (Fig. 2(a) and (b),

respectively). The result of this linear combination is quantity X_V [Fig. 2(c)] that is much less sensitive to rain than $Tb_{\mathrm{Vpol,6\,GHz}}$ and $Tb_{\mathrm{Vpol,10\,GHz}}$. Moreover, Fig. 3 shows the sensitivity of AMSR2 6-, 10-, and 18-GHz H- and V-pol channels to SSW (Fig. 3(a)–(f), where the magenta line is the linear fit shown for reference) and rain [Fig. 3(g)–(l)]. The legends on the SSW sensitivity plots show the slope and the y-intercept of the linear fit. In addition, the legends on all the plots show the Pearson correlation coefficient (R) between the AMSR2 channel and the corresponding geophysical parameter (SSW or rain). Color denotes number of points as shown in the color bar. The plots in Fig. 3 clearly show the strong rain signal embedded in the measured Tbs at these channels.

The three empirical quantities (ζ_1, ζ_2, and ζ_3) are depicted as 3-D density plots and shown in Fig. 4. The reason behind the formulation of these quantities in the form described in (1-a), (2-a), and (3-a) is to increase the sensitivity to SSW by examining the slope of the linear fit of the empirical linear combinations as a function of SSW.

Fig. 4(a)–(c) shows the sensitivity of ζ_1, ζ_2, and ζ_3, respectively, to SSW, and Fig. 4(d)–(f) shows the sensitivity to rain. The magenta line is the linear fit, and the blue line is the binned/averaged line both added for reference. When comparing Figs. 3 and 4, it is evident that ζ_1, ζ_2, and ζ_3 are less susceptible to rain (significant reduction in the values of R) while maintaining decent sensitivity to wind induced surface emission. Also, one can notice from Fig. 4(d)–(f) that a positive slope exists for RRs of $\geq\approx$15 mm/h, indicating that either high RRs are in fact associated with high SSW, or a small residual rain signal still exists in the derived empirical quantities.

2) Regression Technique: The GAWS retrieval algorithm is a statistical multiple linear regression of SSW against the empirical quantities ζ_1, ζ_2, and ζ_3. The training dataset consists of 1000 AMSR2 orbits including hurricane over passes from 2013 to 2021 to cover all day/night and seasonal variability. GDAS and HWRF data were fused together to create a hybrid training dataset after being spatially and temporally interpolated to AMSR2 measurements' locations. Whenever HWRF wind fields exist, they replace GDAS data points for that storm. This provided a consistent and more comprehensive training dataset when compared with scarce in situ measurements. Moreover, AMSR2 is a polar orbiter, and collocations with other polar orbiting earth observing systems will limit the training dataset to high latitudes.

The regression consists of two stages. The first-stage regression coefficients are modeled as a function of SST, since surface emissivity and the absorption by CLW depend on it. The statistical model function is mathematically described in (5), and the regression coefficients C_0, C_1, C_2, and C_3 are shown in Fig. 5 as a function of SST

$$\mathrm{SSW}_{\mathrm{stage1}} = C_0(\mathrm{SST}) + C_1(\mathrm{SST}) \times \zeta_1 + C_2(\mathrm{SST}) \times \zeta_2 + C_3(\mathrm{SST}) \times \zeta_3. \quad (5)$$

Since GAWS retrievals are global and span a wide range of SSW regimes, it is beneficial to add a second-stage regression to fine-tune the retrievals [33], where the regression coefficients now depend on wind speed retrievals from first stage. ζ_2 was selected as the only independent variable for the second-stage regression, since it has the highest sensitivity to SSW (biggest slope and correlation with SSW), as shown in Fig. 4(b). The second-stage statistical model function is mathematically described in (6), and the regression coefficients β_0 and β_1 are shown in Fig. 6 as a function of SSW from stage 1

$$\mathrm{SSW}_{\mathrm{stage2}} = \beta_0\left(\mathrm{SSW}_{\mathrm{stage1}}\right) + \beta_1\left(\mathrm{SSW}_{\mathrm{stage2}}\right) \times \zeta_2. \quad (6)$$

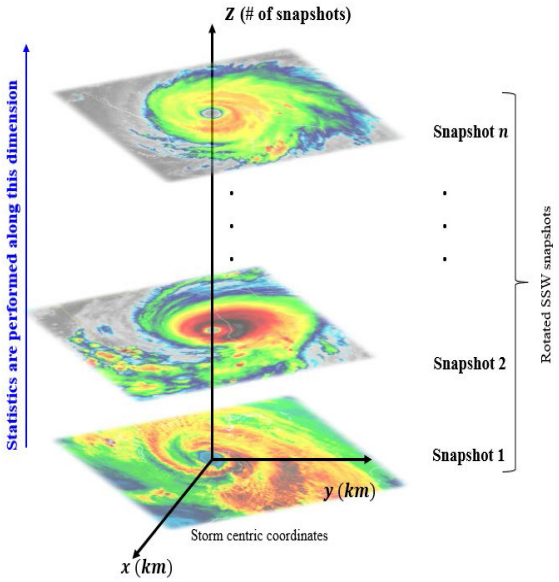

Fig. 11. Depiction of the composite field generation process. Statistics are generated in the vertical (z) direction within cells in the x- and y-directions representing storm-centric coordinates.

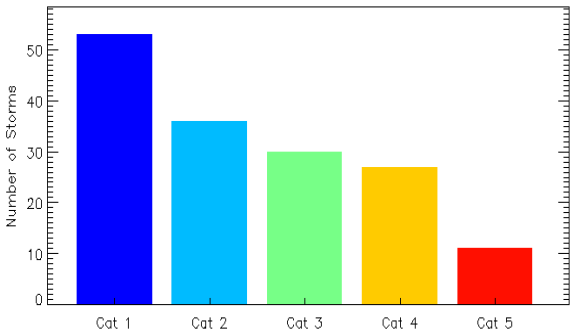

Fig. 12. Categorized number of snapshots used to generate composite plots.

IV. Performance Evaluation

To evaluate the performance of the GAWS retrieval algorithm, two types of validation were conducted, namely: the standard validation and the extreme winds validation. While the standard validation evaluates the overall performance of the GAWS algorithm retrieving global winds, the extreme winds validation evaluates the performance of the GAWS algorithm under extreme wind conditions, such as TCs and ETCs.

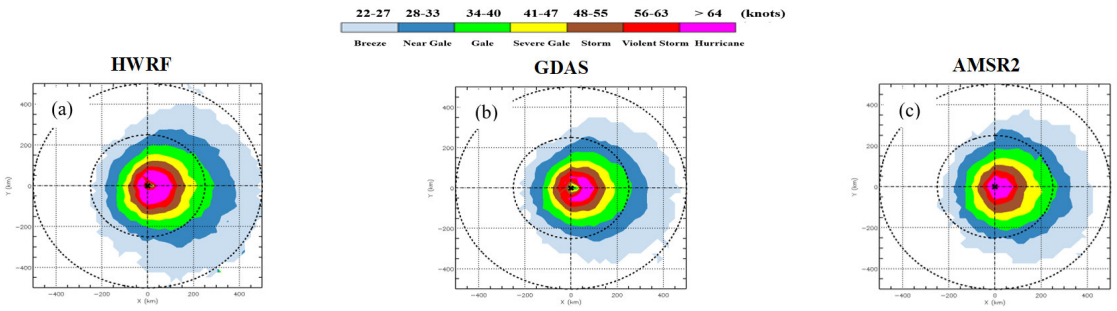

Fig. 13. Composite plots comparison of mean wind speed among (a) HWRF, (b) GDAS, and (c) GAWS applied to AMSR2. Color indicates mean wind speed in knots. The x- and y-axes are the distance (km) away from storm center.

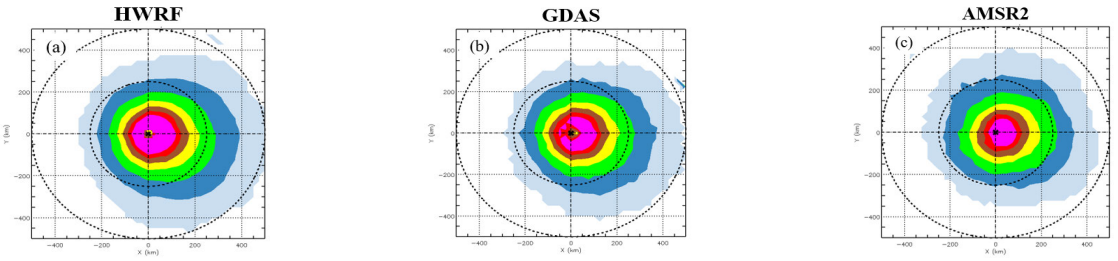

Fig. 14. Similar to Fig. 13 but for major hurricanes only (categories 3–5). (a) HWRF. (b) GDAS. (c) GAWS applied to AMSR2.

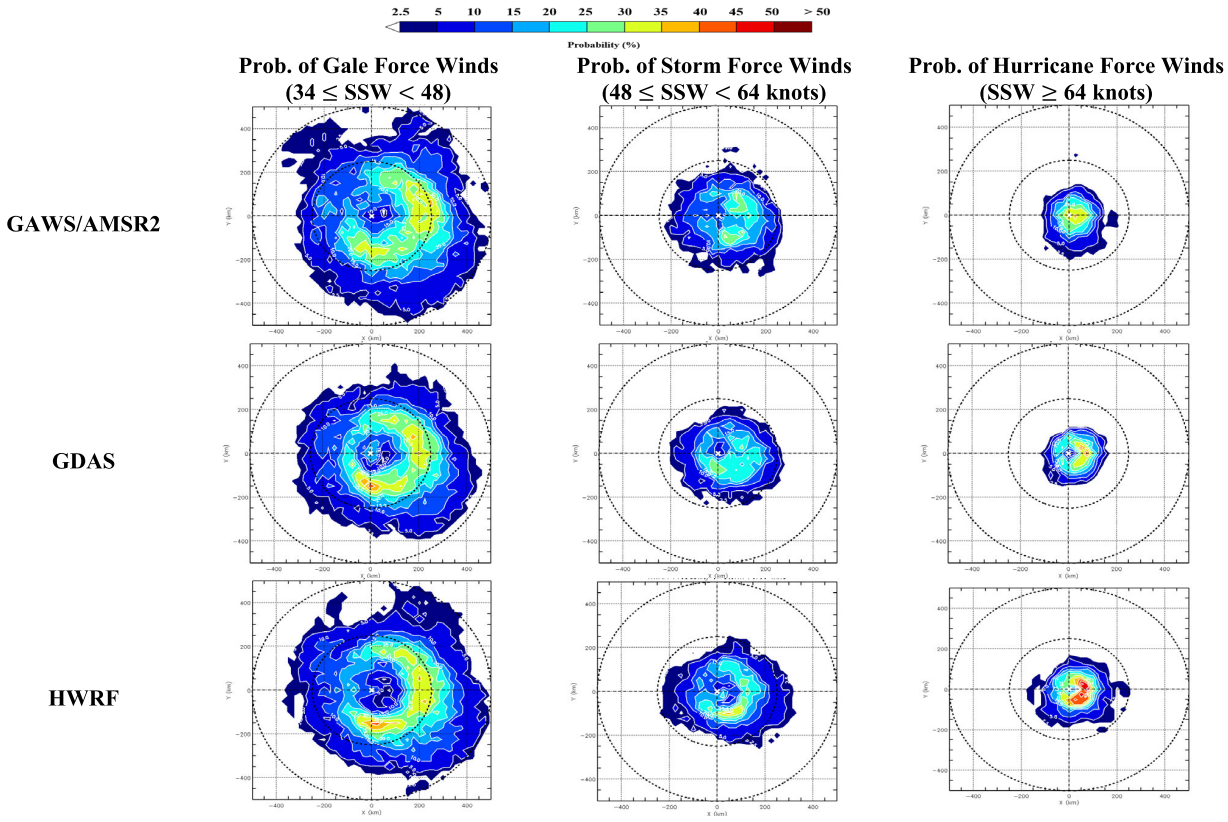

Fig. 15. Composite plots of the probability of hurricane force winds, storm force winds, and gale force winds (columns) for HWRF, GDAS, and GAWS applied to AMSR2 (rows). The x- and y-axes are distance (km) away from storm center.

A. Standard Validation

The standard validation starts with a direct comparison between GAWS retrievals and 0.25° resolution GDAS using 500 independent AMSR2 orbits that were not used in training.

Fig. 7 shows a 3-D density plot where the x-axis is GDAS SSW and the y-axis is AMSR2 GAWS retrievals both in m/s. Histogram for the two quantities being compared is shown as well representing the distribution of wind speeds used in the comparison.

Fig. 8 shows the 3-D density plot of the wind speed error ($\mathrm{SSW_{GAWS}} - \mathrm{SSW_{GDAS}}$) as a function of several AMSR2 sensor parameters [latitude in Fig. 8(a), EIA in Fig. 8(b), cross-scan location (XID) in Fig. 8(c), and relative azimuth (χ) in Fig. 8(d)]. These comparisons will identify any systematic

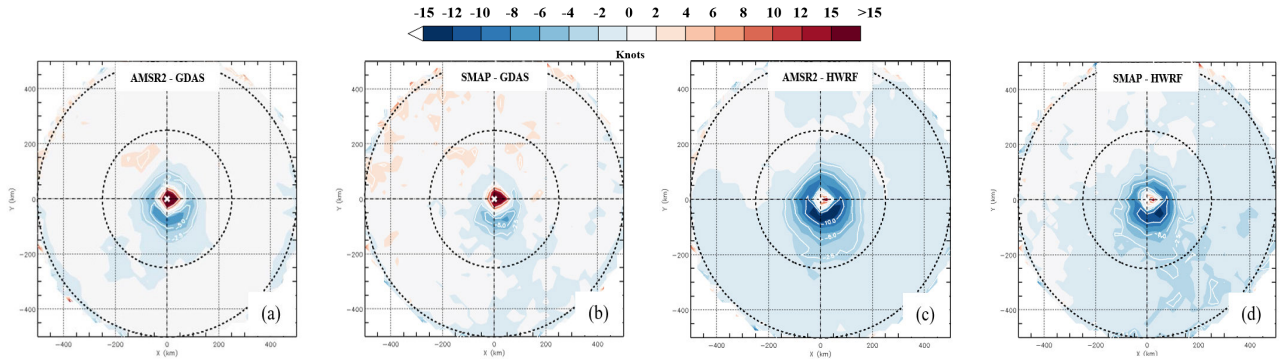

Fig. 16. Composite plots of wind speed error for (a) AMSR2–GDAS, (b) SMAP–GDAS, (c) AMSR2–HWRF, and (d) SMAP–HWRF. The x- and y-axes are the distance (km) away from storm center.

biases in the GAWS retrievals that are a function of these selected parameters. The solid lines represent the mean error, and the dashed line represents the root-mean-square error (RMSE). The mean error for GAWS retrievals is around zero, and the RMSE is <2 m/s for all wind speed regimes.

To validate the performance of GAWS in the presence of precipitation, a comparison of GAWS and advanced scatterometer (ASCAT) wind speed error (m/s) for multiple RRs (mm/h) is shown in Fig. 9 as a function of GDAS wind speed. For ASCAT, we used wind speeds V02.1.1 from Remote Sensing Systems [34]. Among other parameters, this dataset includes ASCAT wind speeds and the collocated radiometer RRs up to 12.5-mm/h spanning low, moderate, and heavy rain. Fig. 9 shows that while ASCAT underestimates wind speeds for high rain and high wind speeds probably due to rain attenuation, GAWS shows slight overestimation of wind speeds at high RRs of >12 mm/h. This could be the result of residual rain signal that was not completely removed from the empirical quantities used in the GAWS retrieval algorithm.

Fig. 10 shows an example of GAWS retrievals in the presence of rain and normal wind conditions. Fig. 10(a) shows AMSR2 RR in mm/h; Fig. 10(b) shows GAWS applied to AMSR2 in m/s, and Fig. 10(c) shows GDAS wind speed (in m/s) for reference. It is evident that in the regions of precipitation, the retrieved SSW does not show any overestimation of SSW, when compared with GDAS, due to the increase of surface emission.

B. Extreme Winds Validation

For extreme winds validation, composite plots will be used to validate the performance of GAWS under such conditions. As the name implies, a composite plot is a compound of several subfields, or "snapshots," of SSW retrievals in storms. These snapshots are defined by a circle with a specified radius from the center of a storm obtained from the IBTrACS database. The IBTrACS data are provided in a 3-h grid and is adjusted by linear interpolation to AMSR2 acquisition time.

The first step in generating SSW composite fields is to put all snapshots in a storm-centric coordinate system. Then, all snapshots are rotated, by different angles corresponding to storm motion direction calculated from IBTrACS, so that the direction of storm motion is always toward the top of the image. Subsequently, the rotated storm-centric snapshots are stacked with the center point being the center position estimate interpolated to the sensor's mean time. This can be imagined in a 3-D space (x, y, z), as shown in Fig. 11. The x- and y-dimensions are the storm-centric coordinates, and the z-dimension represents the stacked snapshots after being rotated. Once these snapshots are stacked, they can be composited, and statistical measures (e.g., mean, median, maximum, and so on) can be computed along the stacking dimension (z) without losing the spatial distribution of the error, as it is the case in scatter plots and histograms.

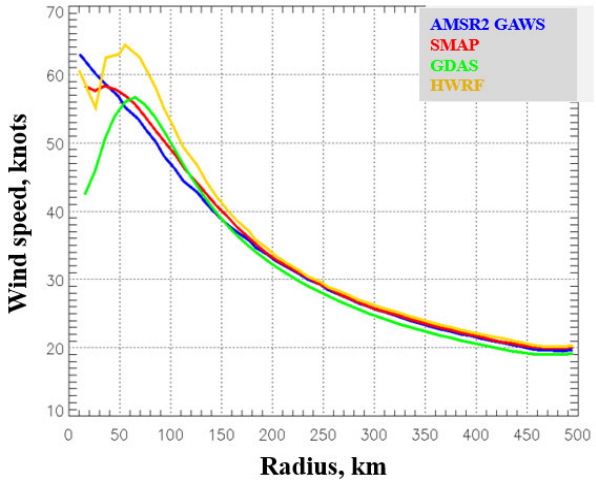

Fig. 17. Wind speed comparison, in knots, as a function of radial distance from storm center for HWRF (yellow), GDAS (green), SMAP (red), and GAWS applied to AMSR2 (blue).

For this study, snapshots data are limited to $\pm$90-min time difference between IBTrACS interpolated time and the sensor acquisition time, and within a circle of 500-km radius around the interpolated storm center position from IBTrACS.

The snapshot data are gridded into a storm-centric common grid with a $25\times25-$km cell size. The composite plots analyses were generated using $\approx$160 snapshots from 2013 to 2021 and include hurricanes from category 1 up to category 5, as shown in Fig. 12.

Fig. 13 shows the composite fields comparison of mean SSW (in knots) among HWRF [Fig. 13(a)], GDAS [Fig. 13(b)] and GAWS applied to AMSR2 [Fig. 13(c)]. Colored contours

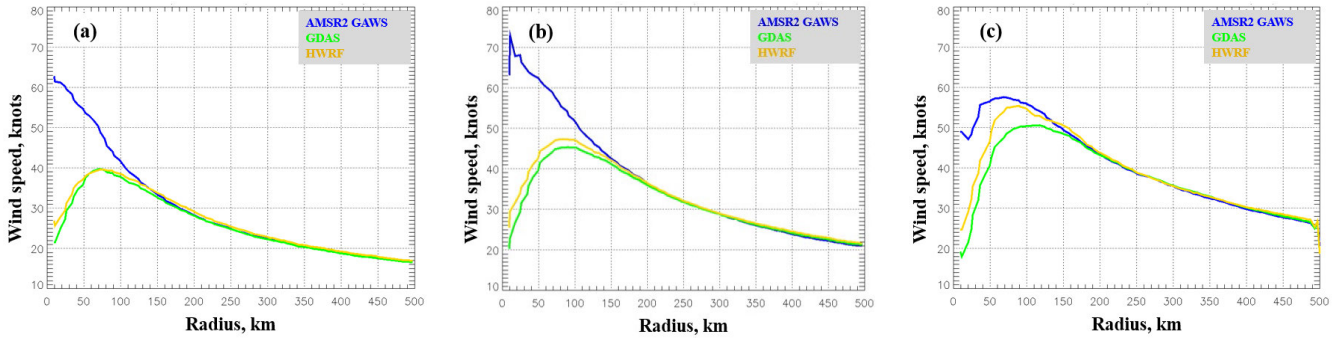

Fig. 18. Wind speeds (in knots) as a function of radial distance from storm center for HWRF (yellow), GDAS (green), and GAWS applied to AMSR2 (blue) for TCs with RMW (a) ≤25 km, (b) between 25 and 50 km, and (c) ≥75 km.

indicate storm type from breeze (22–27 knots) up to hurricane force winds (>64 knots). From Fig. 13, one can notice the comparable sizes of the colored contours between all products. In particular, maximum winds from HWRF, GDAS, and AMSR2 are clustered in the right quadrants of the composite plots where forward motion contributes to the rotation of the storm. Moreover, while HWRF has the biggest hurricane force winds area (biggest purple contour), GDAS and AMSR2 have comparable purple contours.

This is not surprising and can be attributed to multiple factors. First, the original resolution of the HWRF model (≈10 km) is higher than that of GDAS and AMSR2. Second, HWRF and GDAS generation time matches the originally reported IBTrACS samples every 3 h, while AMSR2 overpasses time can vary. Third, HWRF is specially tailored to model SSW in TCs, while GDAS and GAWS are global data products.

Another reason that can attribute to the differences in these contours is the eye of the storm. While HWRF and GDAS can clearly show the eye for all storm sizes, AMSR2 cannot, due to the use of low-frequency channels, with relatively large IFOVs, in the GAWS retrieval algorithm.

Fig. 14 is similar to Fig. 13 but using snapshots of major hurricanes only (categories 3–5). It consists of 68 snapshots and shows a comparable performance of GAWS to that shown in Fig. 14 when hurricanes from all categories (categories 1–5) were included. This indicates the consistent performance of GAWS for all TC categories.

One more important metric calculated from the composited snapshots is the probability of winds. Fig. 15 shows the probability of hurricane force winds (first column), storm force winds (second column), and gale force winds (third column) for GAWS applied to AMSR2 (first row), GDAS (second row), and HWRF (third row), where color indicates the probability of occurrence. While there are slight differences between the calculated probabilities, the spatial distribution is comparable, indicating the efficacy of GAWS to retrieve extreme winds where they occur.

To further examine GAWS performance, it was compared with wind speeds derived from the soil moisture active passive (SMAP). SMAP was chosen for this comparison, because it operates in the L-band range, and it should be less susceptible to rain effects. Fig. 16 shows the composite plots of the error in the retrieved wind speeds when compared with GDAS [Fig. 16(a) and (b)] and when compared with HWRF [Fig. 16(c) and (d)]. For SMAP, we used wind speeds V1.0 from Remote Sensing Systems [35]. It is obvious that the magnitude and the spatial distribution of the error are alike between the two sensors especially inside the 250-km circle where most of the high wind speeds, high RRs, and rapidly changing wind direction take place.

Moreover, Fig. 17 shows a comparison between AMSR2 and SMAP wind speeds as a function of radial distance from the center of the storm. The wind speeds from all quadrants were averaged in 10-km steps and plotted as a point on the curve. The curves start to deviate from each other when the distance is ≈150 km away from the storm center corresponding to the eyewall region of the TC. It is worth noting that the differences between the instruments' original resolutions and times of the overpasses can attribute to the differences between sensors in Figs. 16 and 17.

As mentioned in Section III, GAWS exploits the linear combination of AMSR2 6-, 10-, and 18-GHz channels, with IFOV size up to ≈60 km for the 6-GHz channel. To demonstrate the effect of AMSR2 channels resolution on GAWS performance, Fig. 18 shows GAWS (blue curve), HWRF (yellow curve), and GDAS (green curve) wind speeds as a function of radial distance from the center of the storm. The curves are created from snapshots of TCs (categories 1–5) in a similar fashion to Fig. 17 where wind speeds from all quadrants were averaged in 10-km steps and plotted as a point on the curve. Fig. 18(a) represents the TCs with radius of maximum winds (RMW; obtained from IBTrACS) ≤25 km, Fig. 18(b) for TCs with RMW between 25 and 50 km, and Fig. 18(c) for TCs with an RMW of ≥75 km. The impact of resolution is clear in the ability of the wind retrieval algorithm to detect the eye of the storm [Fig. 18(c)] when the blue curve starts to dip down at around ≈50 km away from the storm center, versus the case in Fig. 18(a) and (b) where the size of the eye is smaller than the IFOV size of AMSR2 C-band channels.

V. Summary

This article described the development and validation of a new operational global all-weather wind speed retrieval algorithm. This new all-weather wind speed product has the

capability to extend the utility of microwave radiometer measurements to areas of heavy precipitation and can be used to retrieve global wind speeds, including hurricane force winds.

The new algorithm, GAWS, is statistical-based and consists of two-stage multiple linear regression. The first-stage regression coefficients are a function of SST, and the second-stage regression coefficients are a function of the retrieved SSW from first stage. The regression was trained using 1000 AMSR2 orbits including hurricane overpasses and a hybrid dataset of GDAS and HWRF fused together as the assumed surface truth.

The independent variables fed to the regression are empirical quantities derived from the linear combinations of AMSR2 6-, 10-, and 18-GHz H- and V-pol channels. These linear combinations of channels are much less susceptible to rain, which allows retrieving SSW even in the presence of heavy precipitation.

The operational implementation of GAWS will complement the set of standard satellite data products and will help scientists and forecasters to further analyze parts of the storms that were previously challenging. Furthermore, GAWS can play an important role in cyclogenesis studies and in the training of future SSW retrieval algorithms using machine learning techniques.

ACKNOWLEDGMENT

The scientific results and conclusions, as well as any views or opinions expressed herein, are those of the authors and do not necessarily reflect those of National Oceanic and Atmospheric Administration (NOAA), College Park, MD, USA, or the Department of Commerce.

REFERENCES

[1] J. Yang et al., "The role of satellite remote sensing in climate change studies," *Nature Climate Change*, vol. 3, no. 10, pp. 875–883, Oct. 2013, doi: 10.1038/nclimate1908.

[2] E. Chuvieco, *Earth Observation of Global Change: The Role of Satellite Remote Sensing in Monitoring the Global Environment*. Berlin, Germany: Springer, 2008.

[3] G. Gutman and J. G. Masek, "Long-term time series of the Earth's land-surface observations from space," *Int. J. Remote Sens.*, vol. 33, no. 15, pp. 4700–4719, 2012, doi: 10.1080/01431161.2011.638341.

[4] N. C. Grody, "Remote sensing of atmospheric water content from satellites using microwave radiometry," *IEEE Trans. Antennas Propag.*, vol. AP-24, no. 2, pp. 155–162, Mar. 1976.

[5] T. T. Wilheit and A. T. C. Chang, "An algorithm for retrieval of ocean surface and atmospheric parameters from the observations of the scanning multichannel microwave radiometer," *Radio Sci.*, vol. 15, no. 3, pp. 525–544, May 1980.

[6] S. O. Alsweiss, Z. Jelenak, and P. S. Chang, "Remote sensing of sea surface temperature using AMSR-2 measurements," *IEEE J. Sel. Topics Appl. Earth Observ. Remote Sens.*, vol. 10, no. 9, pp. 3948–3954, Sep. 2017.

[7] S. Alsweiss, R. Hanna, P. Laupattarakasem, W. Jones, C. Hennon, and R. Chen, "A non-MLE approach for satellite scatterometer wind vector retrievals in tropical cyclones," *Remote Sens.*, vol. 6, no. 5, pp. 4133–4148, May 2014.

[8] S. O. Alsweiss, P. Laupattarakasem, and W. L. Jones, "A novel Ku-band radiometer/scatterometer approach for improved oceanic wind vector measurements," *IEEE Trans. Geosci. Remote Sens.*, vol. 49, no. 9, pp. 3189–3197, Sep. 2011.

[9] M. A. Cane, S. E. Zebiak, and S. C. Dolan, "Experimental forecasts of El Niño," *Nature*, vol. 321, pp. 827–832, Jan. 1986, doi: 10.1038/321827a0.

[10] M. J. McPhaden, "Genesis and evolution of the 1997–98 El Niño," *Science*, vol. 283, no. 5404, pp. 950–954, Feb. 1999, doi: 10.1126/science.283.5404.950.

[11] T. Meissner and F. Wentz, "Ocean retrievals for WindSat: Radiative transfer model, algorithm, validation," in *Proc. IEEE Int. Geosci. Remote Sens. Symp.*, San Juan, Puerto Rico, 2006, pp. 130–133.

[12] T. Meissner and F. J. Wentz, "Wind retrievals under rain for passive satellite microwave radiometers and its application to hurricane tracking," in *Proc. Microw. Radiometry Remote Sens. Environ.*, Mar. 2008, pp. 1–4, doi: 10.1109/MICRAD.2008.4579492.

[13] K. A. Hilburn and F. J. Wentz, "Intercalibrated passive microwave rain products from the unified microwave ocean retrieval algorithm (UMORA)," *J. Appl. Meteorol. Climatol.*, vol. 47, no. 3, pp. 778–794, Mar. 2008.

[14] *JAXA GCOM-W1*. Accessed: Jun. 8, 2022. [Online]. Available: http://suzaku.eorc.jaxa.jp/GCOM_W/w_amsr2/whats_amsr2.html

[15] K. Imaoka, T. Sezai, T. Takeshima, T. Kawanishi, and A. Shibata, "Instrument characteristics and calibration of AMSR and AMSR-E," in *Proc. IEEE Int. Geosci. Remote Sens. Symp.*, Kyoto, Japan, 2010, vol. 38, pp. 18–20.

[16] *AMSR-E Instrument Description*. Accessed: Jun. 8, 2022. [Online]. Available: https://space.oscar.wmo.int/instruments/view/amsr_e

[17] S. O. Alsweiss, Z. Jelenak, P. S. Chang, J. D. Park, and P. Meyers, "Intercalibration results of the advanced microwave scanning radiometer-2 over ocean," *IEEE J. Sel. Topics Appl. Earth Observ. Remote Sens.*, vol. 8, no. 9, pp. 4230–4238, Sep. 2015.

[18] P. C. Meyers and R. R. Ferraro, "Precipitation from the advanced microwave scanning radiometer 2," *IEEE J. Sel. Topics Appl. Earth Observ. Remote Sens.*, vol. 9, no. 6, pp. 2611–2618, Jun. 2016, doi: 10.1109/JSTARS.2015.2513666.

[19] S. Alsweiss, J. Sapp, Z. Jelenak, and P. Chang, "An operational all-weather wind speed from AMSR2," in *Proc. IEEE Int. Geosci. Remote Sens. Symp.*, Jul. 2021, pp. 7334–7337, doi: 10.1109/IGARSS47720.2021.9553710.

[20] *NOAA's GCOM-W Program Products Webpage*. Accessed: Jun. 8, 2022. [Online]. Available: https://manati.star.nesdis.noaa.gov/gcom/datasets/GCOM2Data.php

[21] *AMSR-2 Level1 Product*. Accessed: Jun. 13, 2022. [Online]. Available: https://gportal.jaxa.jp/gpr/assets/mng_upload/GCOM-W/AMSR2_Level1_Product_Format_EN.pdf

[22] D. T. Kleist, D. F. Parrish, J. C. Derber, R. Treadon, W. Wu, and S. Lord, "Introduction of the GSI into the NCEP global data assimilation system," *Weather Forcasting*, vol. 24, no. 6, pp. 1691–1705, 2009, doi: 10.1175/2009WAF2222201.1.

[23] *National Center for Environmental Prediction GDAS Webpage*. Accessed: Jun. 14, 2022. [Online]. Available: https://www.emc.ncep.noaa.gov/gmb/gdas/

[24] *National Center for Environmental Prediction HWRF Webpage*. Accessed: Jun. 14, 2022. [Online]. Available: https://www.emc.ncep.noaa.gov/gc_wmb/vxt/HWRF/index.php

[25] M. K. Biswas. (2018). *Hurricane Weather Research and Forecasting (HWRF) Model: 2018 Scientific Documentation*. Accessed: Jun. 14, 2022. [Online]. Available: https://dtcenter.org/HurrWRF/users/docs/index.php

[26] K. R. Knapp, M. C. Kruk, D. H. Levinson, H. J. Diamond, and C. J. Neumann, "The international best track archive for climate stewardship (IBTrACS): Unifying tropical cyclone data," *Bull. Amer. Meteorolog. Soc.*, vol. 91, no. 3, pp. 363–376, Mar. 2010, doi: 10.1175/2009BAMS2755.1.

[27] K. R. Knapp, H. J. Diamond, J. P. Kossin, M. C. Kruk, and C. J. Schreck, "International best track archive for climate stewardship (IBTrACS) project, version 4.0," U.S. Dept. Commerce, NESDIS, NOAA, Nat. Centers Environ. Inf., Asheville, North Carolina, Tech. Rep., 2022, doi: 10.25921/82ty-9e16.

[28] T. Meissner and F. Wentz, "An updated analysis of the ocean surface wind direction signal in passive microwave brightness temperature," *IEEE Trans. Geosci. Remote Sens.*, vol. 40, no. 6, pp. 1230–1240, Jun. 2002.

[29] S. Soisuvarn, Z. Jelenak, and W. L. Jones, "An ocean surface wind vector model function for a spaceborne microwave radiometer," *IEEE Trans. Geosci. Remote Sens.*, vol. 45, no. 10, pp. 3119–3130, Oct. 2007.

[30] S. Alsweiss, Z. Jelenak, and P. Chang, "All-weather geophysical model function for wind speed retrievals from AMSR2," in *Proc. IEEE Int. Geosci. Remote Sens. Symp.*, Jul. 2022, pp. 6915–6918, doi: 10.1109/IGARSS46834.2022.9884002.

[31] T. Meissner and F. J. Wentz, "The emissivity of the ocean surface between 6 and 90 GHz over a large range of wind speeds and Earth incidence angles," *IEEE Trans. Geosci. Remote Sens.*, vol. 50, no. 8, pp. 3004–3026, Aug. 2012, doi: 10.1109/TGRS.2011.2179662.

[32] T. Meissner, L. Ricciardulli, and A. Manaster, "Tropical cyclone wind speeds from WindSat, AMSR and SMAP: Algorithm development and testing," *Remote Sens.*, vol. 13, no. 9, p. 1641, Apr. 2021, doi: 10.3390/rs13091641.

[33] F. Wentz and T. Meissner, "Algorithm theoretical basis document (ATBD), supplement 1, AMSR ocean algorithm," Remote Sensing Systems, Santa Rosa, CA, USA, Tech. Rep., 1051707, 2006. Accessed: Jun. 22, 2022. [Online]. Available: http://images.remss.com/papers/rsstech/2007_051707_Wentz_AMSR_Ocean_Algorithm_Version_2_Supplement1_ATBD.pdf

[34] *ASCAT Wind Speeds Product Description Webpage*. Accessed: Feb. 10, 2022. [Online]. Available: https://www.remss.com/missions/ascat/

[35] *SMAP Wind Speeds Product Description Webpage*. Accessed: Aug. 20, 2022. [Online]. Available: https://www.remss.com/missions/smap/winds/

Suleiman Alsweiss (Senior Member, IEEE) received the Ph.D. degree in electrical engineering from the University of Central Florida (UCF), Orlando, FL, USA, in 2011.

He joined the Ocean Winds Science Team at National Oceanic and Atmospheric Administration (NOAA)/National Environmental Satellite, Data and Information Service (NESDIS)/STAR, College Park, MD, USA, as a Scientist with Global Science and Technology Inc. (GST), Greenbelt, MD, USA. His research interests include active and passive sensors calibration and advanced satellite data products development and validation.

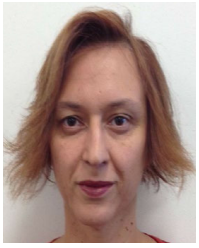

Zorana Jelenak (Member, IEEE) received the Ph.D. degree in physics from Waikato University, Hamilton, New Zealand, in 2000.

Since 2001, she has been a Project Scientist at University Corporation for Atmospheric Research (UCAR), Boulder, CO, USA, and a member of the Ocean Winds Team at National Oceanic and Atmospheric Administration (NOAA)/National Environmental Satellite, Data and Information Service (NESDIS)/STAR, College Park, MD, USA. Her research interests include ocean remote sensing from active and passive microwave airborne and spaceborne instruments, with an emphasis on ocean wind and wave measurements. Of particular interest is data applicability in an operational near-real-time environment, retrieval algorithm development, model function development, and advanced statistical analysis and error analysis for improved product and retrieval algorithm characterization.

Paul S. Chang (Senior Member, IEEE) received the Ph.D. degree in electrical engineering from the University of Massachusetts Amherst, Amherst, MA, USA, in 1994.

Since 1994, he has been a Research Physical Scientist at the Center for Satellite Applications and Research (STAR), National Environmental Satellite, Data and Information Service (NESDIS), National Oceanic and Atmospheric Administration (NOAA). College Park, MD, USA. His research interests include research and development in active and passive microwave remote sensing of the ocean surface with an emphasis on retrieval of the ocean surface wind field. Wind retrieval algorithm improvements and new product developments are pursued through the analyses of satellite and aircraft microwave remote sensing data. An emphasis is placed on transitioning research results into operational use, which involves cooperative relationships with the operational facets of NESDIS and with the National Weather Service, a primary end user of this data.